



MMS Observations of Whistler-Mode Waves: Comparison Between the Observed and Theoretically Predicted Electric Field

Downloaded from: <https://research.chalmers.se>, 2026-05-10 17:56 UTC

Citation for the original published paper (version of record):

Hartley, D., Christopher, I., Argall, M. et al (2026). MMS Observations of Whistler-Mode Waves: Comparison Between the Observed and Theoretically Predicted Electric Field. *Journal of Geophysical Research: Space Physics*, 131(3).
<http://dx.doi.org/10.1029/2025JA034885>

N.B. When citing this work, cite the original published paper.

JGR Space Physics

RESEARCH ARTICLE

10.1029/2025JA034885

Key Points:

- Novel analysis reveals the Magnetospheric MultiScale whistler-mode wave electric field shows a density-dependent response consistent with sheath impedance effects
- Both the spin-plane and spin-axis measurements show systematic, and sometimes large, amplitude and phase deviations
- These deviations directly influence computation of energy exchange rates, potentially leading to misinterpretation of wave-particle dynamics

Supporting Information:

Supporting Information may be found in the online version of this article.

Correspondence to:

D. P. Hartley,
david-hartley@uiowa.edu

Citation:

Hartley, D. P., Christopher, I. W., Argall, M. R., Ahmadi, N., Santolík, O., Kolmašová, I., et al. (2026). MMS observations of whistler-mode waves: Comparison between the observed and theoretically predicted electric field. *Journal of Geophysical Research: Space Physics*, 131, e2025JA034885. <https://doi.org/10.1029/2025JA034885>

Received 17 NOV 2025

Accepted 27 FEB 2026

© 2026. The Author(s).

This is an open access article under the terms of the [Creative Commons Attribution License](#), which permits use, distribution and reproduction in any medium, provided the original work is properly cited.

MMS Observations of Whistler-Mode Waves: Comparison Between the Observed and Theoretically Predicted Electric Field

D. P. Hartley¹, I. W. Christopher¹, M. R. Argall², N. Ahmadi³, O. Santolík^{4,5}, I. Kolmašová^{4,5}, Y. V. Khotyaintsev^{6,7}, and I. Svenningsson^{6,7,8}

¹Department of Physics and Astronomy, University of Iowa, Iowa City, IA, USA, ²Space Science Center, Institute for the Study of Earth, Oceans, and Space, University of New Hampshire, Durham, NH, USA, ³Laboratory for Atmospheric and Space Physics, University of Colorado, Boulder, CO, USA, ⁴Department of Space Physics, Institute of Atmospheric Physics, Prague, Czech Republic, ⁵Faculty of Mathematics and Physics, Charles University, Prague, Czech Republic, ⁶Swedish Institute of Space Physics, Uppsala, Sweden, ⁷Department of Physics and Astronomy, Uppsala University, Uppsala, Sweden, ⁸Department of Physics, Chalmers University of Technology, Göteborg, Sweden

Abstract Electric field instruments function by electrically coupling to the surrounding plasma, resulting in a response function that varies depending on local conditions. This variable coupling can complicate quantitative interpretation of wave measurements, yet is rarely considered. While this effect has recently been quantified for the Van Allen Probes, we present the first quantitative analysis for the Magnetospheric MultiScale (MMS) mission. First, MMS observations are evaluated against Faraday's Law, revealing that the angle between the measured whistler-mode electric and magnetic fields directly depends on the wave propagation direction, a feature consistent with sheath impedance effects. A novel technique for determining electric field observations along each measurement direction is introduced, addressing limitations of previous works. This reveals that, for MMS in low-density plasma, spin-plane amplitudes are ~60% of expected values, with small phase shifts, while spin-axis measurements are accurate within 5%–10%, with phase shifts up to -20° . At intermediate densities, spin-plane amplitudes match, or slightly exceed, expected values whereas spin-axis observations can be overestimated by 70% and experience frequency-dependent phase shifts. At high-density, spin-plane measurements generally agree with expected values, but spin-axis observations are overestimated by ~30% and experience ~30° phase shifts. Accurate measurements are critical, with electric field fluctuations increasingly being used to infer wave-particle energy exchange rates. If electric field observations can be under or over-measured depending on the local plasma environment, this directly impacts these computations of energy exchange rates, potentially leading to a misinterpretation of the fundamental physical mechanisms that drive particle dynamics.

1. Introduction

In situ measurements of the electric field associated with the various different plasma waves in near Earth space are often made by spherical double probe sensors (e.g., Bonnell et al. (2008); Ergun et al. (2001, 2016); Gustafsson et al. (1997); Harvey et al. (1995); Lindqvist et al. (2016); Marklund (1993); Marklund et al. (2004); Mozer (1973); Mozer et al. (1979); Wygant et al. (1992, 2013)). These sensors, mounted on the end of long booms, measure the potential difference, ΔV , between two points separated by distance, ΔL , with the electric field given as $\Delta V/\Delta L$ (e.g., Gurnett (1998)). In many conditions ΔL is the separation distance between the two sensors, however, in some circumstances a shorting factor may need to be considered, where the effective separation of the sensors shrinks to some fraction of the physical probe separation (e.g., Bonnell et al. (2008); Califf and Cully (2016); Cully (2007); Khotyaintsev et al. (2014); Lejosne and Mozer (2019); Mozer et al. (1974); Pedersen et al. (1998)). Short-wavelength effects may also need to be considered when the wavelength becomes comparable to the probe separation (e.g., Gurnett (1998); Lalti et al. (2023)). With electric field sensors measuring the potential difference, they are electrically coupled to the plasma environment in which they operate (e.g., Fahlson (1967); Storey (1963)). This leads to a coupling function at the instrument-plasma interface that varies depending on the local conditions, often represented as a voltage divider with complex impedance (e.g., Bale et al. (2008); Boehm et al. (1994); Koons et al. (1970)). During ground calibrations prior to launch, it is difficult to establish the exact nature of this response function over the full range of conditions that

will be encountered on-orbit. As such, some degree of uncertainty exists in electric field measurements made using space-based infrastructure.

Attempts have been made to quantify how the Van Allen Probes (Mauk et al., 2012) Electric Field and Waves (EFW) instrument (Wygant et al., 2013) coupling function varies with local plasma density and wave frequency, uncovering a response largely consistent with sheath impedance effects (Hartley et al., 2015, 2016, 2017), and ultimately leading to a sheath impedance model, and a sheath-corrected data product (Hartley, Christopher, et al., 2022; Hartley et al., 2023; Kletzing et al., 2023). Here, a similar investigation is performed for Magnetospheric Multiscale (MMS) observations (Burch et al., 2016), by first following a similar methodology as used for the initial Van Allen Probes investigation. This work implements data from the FIELDS instrumentation suite (Torbert et al., 2016), specifically the Electric Double Probes (EDP) along the spin-axis (ADP) (Ergun et al., 2016) and the spin-plane (SDP) (Lindqvist et al., 2016), the Search Coil Magnetometer (SCM) (Le Contel et al., 2016), and the Fluxgate Magnetometer (Russell et al., 2016), in addition to data from the Fast Plasma Investigation (FPI) (Pollock et al., 2016). Subsequently, a significantly revised technique is presented that removes some key limitations of previous work. This improved methodology permits a solution under a broader range of conditions, and allows for a more detailed investigation of the response of each antenna direction of the electric field instrumentation.

Gaining a more complete understanding of the measurements already being taken in near-Earth space is crucial, given that several recent studies directly use the measured fluctuations in the electric field to determine energy transfer rates between waves and particles for various different modes of plasma wave (e.g., Afshari et al. (2021, 2024); Chen et al. (2019); Liu (2025)). Over- and/or under-measurement of the wave electric field will directly impact these energy exchange computations, and may lead to misplaced interpretation of the fundamental physical mechanisms that drive particle dynamics in the terrestrial magnetosphere, and beyond.

2. Identification of Whistler-Mode Waves

MMS utilizes automated burst mode triggers and a Scientist In The Loop (SITL) to examine low-resolution survey data, and actively select and classify burst mode intervals of interest to prioritize for downlink to the ground. As part of this process the SITL writes a brief description of each interval that is publicly available and searchable (<https://lasp.colorado.edu/mms/sdc/public/about/events/>). Whistler-mode waves are identified in the MMS burst data by initially surveying these SITL descriptions for the keywords “whistler” and “chorus.” These time periods have been supplemented with some additional periods of data, with a full list of the 1,757 burst mode intervals used in this study provided in Supporting Information S1. Wave polarization and propagation characteristics are determined from SCM data for these intervals using Singular Value Decomposition (SVD) (Santolík et al., 2003). To extract whistler-mode waves from these intervals, we only consider; (a) frequencies between the local proton cyclotron frequency and the local electron cyclotron frequency; (b) waves where the ellipticity and planarity both exceed 0.7 (Santolík et al., 2002), to ensure right-handed polarization with a well-defined wave normal direction; and (c) waves where the magnetic field wave power spectral density exceeds 10^{-7} nT²/Hz, to ensure signal sufficiently above the instrument background levels. These criteria are similar to previous studies of whistler-mode waves (e.g., Bingham et al. (2018); Hartley et al. (2018, 2019, 2025); Hartley, Chen et al., 2022; Li et al. (2014, 2016); Svenningsson et al. (2022, 2024)) and are used to create the wave database used in the subsequent analysis. To provide insight into the spatial, frequency, and density distributions sampled with this whistler-mode wave data set, Figure S1 in Supporting Information S1 provides occurrences in MLT and L shell, a breakdown of occurrences by region as reported by Toy-Edens et al. (2024), as well as probability distributions in density and frequency, for additional context. Here, an occurrence is defined as an unaveraged spectral matrix, $SM(f, t)$, meaning there can be multiple occurrences at a single timestamp, due to a wave spanning multiple frequency channels at a single time instance. This data set comprises of 2,191,612 data points, with 267,799 unique timestamps. Less than 1% of data occur at frequencies below the lower hybrid resonance frequency.

3. The Angle Between the Electric and Magnetic Field Vectors

In Van Allen Probes data, one feature which suggested phase shifts due to sheath impedance effects arose from an examination of the angle between the electric and magnetic field associated with whistler-mode waves (i.e., \mathbf{E}_{wave} and \mathbf{B}_{wave} and not the background magnetic field, \mathbf{B}_0). Here, \mathbf{E}_{wave} and \mathbf{B}_{wave} are complex spectral quantities from the Fast Fourier Transform (FFT) of the waveform. Faraday's Law informs us that, for a single plane wave,

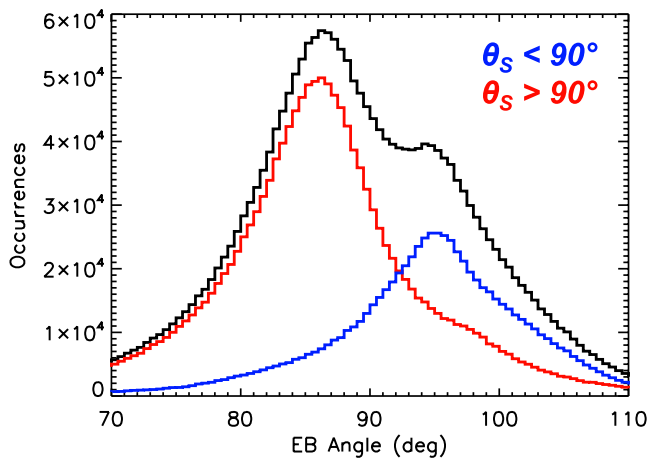


Figure 1. The angle between \mathbf{E}_{wave} and \mathbf{B}_{wave} for (black) all Poynting vector directions, (red) Southward propagating waves, and (blue) Northward propagating waves.

$\mathbf{E}_{\text{wave}} \cdot \mathbf{B}_{\text{wave}} = 0$, meaning that the angle between \mathbf{E}_{wave} and \mathbf{B}_{wave} is 90° . Prior to consideration of sheath impedance effects, the angle between \mathbf{E}_{wave} and \mathbf{B}_{wave} for all planar whistler-mode waves observed by the Van Allen Probes presented a bifurcated distribution with two peaks, one above 90° and one below 90° . A relative minimum in occurrences was observed centered on the expected value of 90° . Each of these peaks corresponded to waves with opposing Poynting vector directions defined by θ_S , where θ_S is the angle between the Poynting vector, \mathbf{S} , and the background magnetic field and is determined from complex spectral estimates (e.g., Santolík et al. (2010); Taubenschuss et al. (2016)). Northward propagating waves ($\theta_S < 90^\circ$) were responsible for the peak in occurrences above 90° and Southward propagating waves ($\theta_S > 90^\circ$) responsible for the peak in occurrences below 90° (Hartley, Christopher, et al., 2022). A schematic of how the angle between \mathbf{E}_{wave} and \mathbf{B}_{wave} can shift in opposite directions away from 90° depending on the Poynting vector direction due to phase shifts from sheath effects is shown in Figure 15 of Hartley et al. (2022a). Here, we perform a similar analysis using data from MMS, with results presented in Figure 1. The black histogram shows whistler-mode wave data for all Poynting vector directions. There is a primary peak in occurrences centered near 85° , a local minima at 90° , and

then a smaller secondary peak in occurrences centered near 95° . This is similar to the features reported using Van Allen Probes data. Next, all whistler-mode waves are separated by their Poynting vector direction, with results overlotted on Figure 1. Southward propagating waves ($\theta_S > 90^\circ$) are shown in red, whereas Northward propagating waves ($\theta_S < 90^\circ$) are shown in blue. The bifurcated distribution that was apparent when considering all whistler-mode waves is clearly separated when sorting based on the Poynting vector direction. Southward propagating waves (red) are clearly the cause of the peak below 90° , and Northward propagating waves (blue) are evidently the source of the peak above 90° . Neither Northward or Southward propagating waves exhibit a secondary peak on the opposing side of 90° from their primary peak. As such, this result is clear evidence that the angle between \mathbf{E}_{wave} and \mathbf{B}_{wave} is shifted above the expected value for Northward propagating waves, and below the expected value for Southward propagating waves. Interestingly, while the bimodal nature of the distribution and the two peaks corresponding to oppositely directed Poynting vector directions is very similar to that observed on Van Allen Probes, the direction is different. For Van Allen Probes, the Northward (Southward) propagating waves were responsible for the peak in occurrences above (below) the expected value of 90° , whereas for MMS it is the opposite.

For Van Allen Probes observations, this effect of a bifurcated distribution in the angle between \mathbf{E}_{wave} and \mathbf{B}_{wave} was attributed to phase shifts in the measured electric field due to sheath impedance effects. That is, for example, a clockwise phase shift in the electric field would result in the angle between \mathbf{E}_{wave} and \mathbf{B}_{wave} being larger than 90° for a wave propagating in one direction past the spacecraft, but would result in an angle less than 90° for a wave propagating in the opposite direction. The reason why the effect is reversed for MMS when compared to Van Allen Probes, is attributed to the different instrument orientation and spin of the spacecraft, with the shorter spin-axis electric field booms being nominally Sunward for Van Allen Probes, and nominally oriented near the ecliptic north pole for MMS. The wave geometry as it propagates past the spacecraft also plays a role. However, in spite of these differences, this result suggests that the electric field observed by MMS is subject to similar antenna-sheath impedance effects as observed on the Van Allen Probes. It is worth noting that the wavelength of whistler-mode waves are large enough that short-wavelength effects need not be considered.

In order to explore this further, a similar approach to that used on the Van Allen Probes is utilized. Following a provisional analysis, a significantly revised approach that removes a number of assumptions used in previous work is also presented, as described in the subsequent sections.

4. Calculating the Theoretically Predicted Electric Field Wave Amplitude and Comparison With Observations

In initial studies based on Van Allen Probes observations, the total electric field wave power summed over all three antenna directions was computed from observations of the magnetic field and cold plasma theory, and compared to the electric field observed by the spacecraft. Since magnetic field observations are not subject to the

same sheath impedance effects as electric field measurements (although other sources of noise and uncertainty do exist, see review by Hospodarsky (2016); Santolík et al. (2025)), considering the ratio between the observed and calculated electric field can provide insight into the on-orbit instrument response. This was initially done assuming parallel propagation of the waves (Hartley et al., 2015), before the wave vector direction was included in the conversion factor (Hartley et al., 2016). Here, we initially follow a similar methodology to that described in Hartley et al. (2016), using MMS observations to compute the total electric field wave amplitude, E_w , from observations of the total magnetic field wave amplitude, B_w , through Equation 1.

$$E_w^2 = \frac{c^2}{n^2} \left(\frac{(P - n^2 \sin^2 \theta_k)^2 \left[\left(\frac{D}{S - n^2} \right)^2 + 1 \right] + (n^2 \cos \theta_k \sin \theta_k)^2}{\left(\frac{D}{S - n^2} \right)^2 (P - n^2 \sin^2 \theta_k)^2 + P^2 \cos^2 \theta_k} \right) B_w^2 \quad (1)$$

where n is the refractive index as defined by Equation 2, and D , L , P , R and S are the Stix parameters (Stix, 1992). The wave normal angle, θ_k is determined using SVD (Santolík et al., 2003) on the magnetic spectral matrix. This yields a 180° ambiguity in the direction of k , which is removed by using the sign of the parallel component of the Poynting vector to place k in the correct hemisphere. As such, θ_k is defined within the full 0° to 180° range.

$$n^2 = \frac{RL \sin^2 \theta_k + PS(1 + \cos^2 \theta_k) - \sqrt{(RL - PS)^2 \sin^4 \theta_k + 4P^2 D^2 \cos^2 \theta_k}}{2(S \sin^2 \theta_k + P \cos^2 \theta_k)} \quad (2)$$

f_{ce} is the electron cyclotron frequency and is determined from the fluxgate magnetometer and f_{pe} is the electron plasma frequency and is calculated using the FPI Dual Electron Spectrometer (DES) electron number density. It is worth noting that FPI DES densities may be a lower limit of the true density inside of the magnetosphere. Since the calculated wave power scales linearly with density, underestimation of the density by a factor of N results in a decrease in the calculated wave power by the same factor, N . When considering amplitudes, this becomes a factor of \sqrt{N} . Exploring use of additional data to reduce this uncertainty, such as densities derived from the upper hybrid resonance frequency, is an avenue of future research.

Only right-hand polarized plane waves which meet the above defined whistler-mode wave identification criteria are considered, with each frequency channel where whistler-mode waves are observed providing a wave amplitude for each time instance. Figure 2 displays a direct comparison between the observed electric field whistler-mode wave amplitude, and that calculated from Equation 1, for (a) plasma density values below 5 cm⁻³, (b) plasma density values between 5 cm⁻³ and 30 cm⁻³, and (c) plasma density values in excess of 30 cm⁻³. Colors indicate the occurrences in each bin, normalized to the maximum number of data points in each column. In this format, if the calculated electric field wave amplitude were always equal to the measured value at each time instance, all data would sit directly on the diagonal line of equivalence.

Figures 2d–2f present probability histograms of the ratio between the observed and calculated electric field whistler-mode wave amplitude for the same three plasma density ranges. Ratios are shown on a logarithmic scale so that values of, for example, 0.2 and 5 appear with the same deviation from a ratio of unity. To provide quantitative comparison, the percentage of data in discreet ratio bins is computed and provided in the colored bands at the top of each panel. These ratio bins are defined as: observed electric field wave amplitude is under-measured by a factor greater than 3 (Ratio < 0.33, dark blue); observed electric field wave amplitude is under-measured by a factor greater than 1.5 but less than 3 (0.33 < Ratio < 0.67, light blue); observed electric field wave amplitude is within a factor of 1.5 of the expected value (0.67 < Ratio < 1.5, green); observed electric field wave amplitude is over-measured by a factor greater than 1.5 but less than 3 (1.5 < Ratio < 3.0, orange); and observed electric field wave amplitude is over-measured by a factor greater than 3 (Ratio > 3.0, red).

In the low density regime below 5 cm⁻³, it is apparent that the measured electric field wave amplitude is less than the calculated electric field wave amplitude in the majority of cases. Figure 2a shows a high concentration of data points offset below the diagonal line of equivalence, particularly below calculated electric field values of 1 mV/m. Interestingly, for larger calculated wave amplitudes in excess of ~1 mV/m, the magnitude of the offset shrinks and the measured electric field wave amplitude is approximately equal to the calculated value. Figure 2d

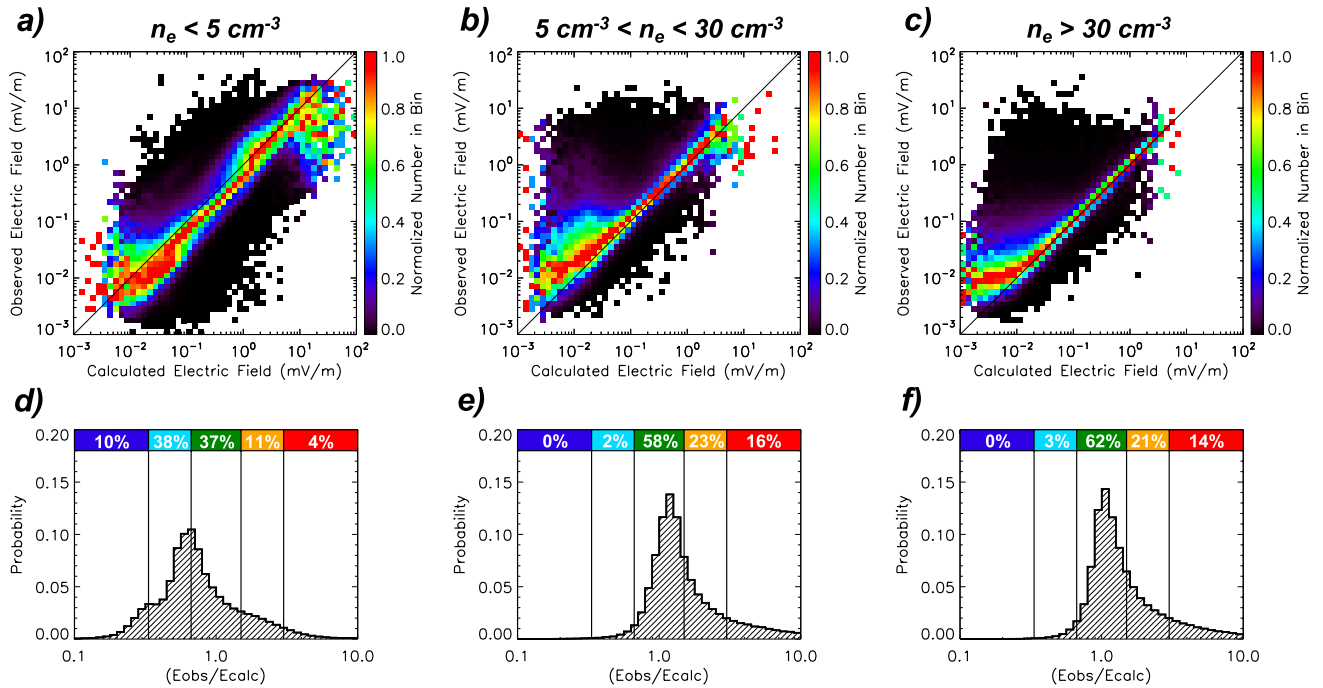


Figure 2. (Top) Direct comparison between observed and calculated electric field wave amplitude with colors indicating the occurrences in each bin normalized to the total occurrences in each column, and (bottom) histograms showing the ratio between the observed and calculated electric field, for (a) and (d) $n_e < 5 \text{ cm}^{-3}$, (b) and (e) $5 \text{ cm}^{-3} < n_e < 30 \text{ cm}^{-3}$, and (c) and (f) $n_e > 30 \text{ cm}^{-3}$.

quantifies the magnitude of the observed offsets, with a peak in occurrences centered around a ratio of 0.7 indicating, on average, a 30% under-measurement of the whistler-mode electric field wave amplitude. Around 48% of wave amplitudes are under-measured by a factor of 1.5 or greater, 37% are within a factor of 1.5 of the expected wave amplitude, and 15% of wave amplitudes are over-measured by a factor of 1.5 or greater.

At intermediate densities between 5 cm^{-3} and 30 cm^{-3} , much closer agreement between the observed and calculated wave amplitude is apparent, with no systematic offset. Figure 2b shows the largest density of data almost directly on, or slightly above the diagonal line of equivalence. Figure 2e highlights the levels of agreement, with the peak in occurrences centered only slightly above a ratio of unity. Under these density conditions, only 3% of wave amplitudes are under-measured by a factor of 1.5 or greater, 58% are within a factor of 1.5 of the expected wave amplitude, and 39% of wave amplitudes are over-measured by a factor of 1.5 or greater. The long tail of the distribution toward ratios greater than unity is attributed to low wave amplitude events, where occurrences slightly above the diagonal line of equivalence become more apparent. Overall, there is a substantially increased level of agreement between the observed and calculated electric field at intermediate densities compared to the low-density regime.

At higher density values, above 30 cm^{-3} , the highest degree of agreement between the observed and calculated wave amplitude is apparent. Figure 2c demonstrates that the majority of data lie almost directly along the diagonal, deviating only slightly for lower wave amplitudes. This is further demonstrated in Figure 2f, which presents a histogram that shows a peak in the ratio between the observed and calculated electric field wave amplitude centered very close to unity. At high-density, only 3% of wave amplitudes are under-measured by a factor of 1.5 or greater, with 62% of data within a factor of 1.5 of the expected value, and 35% of wave amplitudes over-measured by a factor of 1.5 or greater.

This relationship, with the observed and calculated wave amplitudes showing a higher degree of agreement at higher densities, and exhibiting a sometimes substantial under-measurement of the electric field at low densities, is largely consistent with what has been reported based on observations from the Van Allen Probes. Similar to the bifurcated distribution of the angle between \mathbf{E}_{wave} and \mathbf{B}_{wave} , under-measurement of the electric field at low-density is indicative of antenna-sheath impedance effects. For additional context, Figure S2 in Supporting

Information S1 provides occurrences in MLT and L shell, as well as a breakdown of occurrences by region as reported by Toy-Edens et al. (2024), for each of the three density ranges used in this analysis.

5. An Improved Methodology for Computing the Theoretically Predicted Electric Field Wave Amplitude and Phase

Building on the initial results of Hartley et al. (2016), further studies made attempts to distinguish between the electric field observed along each antenna direction of the Van Allen Probes. For example, Hartley et al. (2017) investigated how discrepancies between the observed and calculated electric field were related to how much the spin-axis antenna contributed to the total electric field wave power. Furthermore, Hartley, Christopher et al. (2022) used intervals of favorable geometry between the electric field instrument, the wave, and the background magnetic field to reveal detailed differences between the instrument response in the spin-plane compared to the spin-axis. Here, we build on the methodology used by Hartley, Christopher et al. (2022) and develop a technique for calculating the electric field wave power along each antenna direction for all observations of planar whistler-mode waves, thus removing a limitation of previous work, and providing a more general solution.

This approach may be summarized as:

1. Transform the magnetic field wave complex Fourier coefficients into field-aligned coordinates (z-direction parallel to background magnetic field, B_0 , y-direction defined by the cross product of B_0 and the Earth-to-spacecraft vector, and the x-direction completing the right-handed coordinate system).
2. Rotate observations to field-aligned coordinate system where the wave vector, k , is in the x-z plane. This is done by rotating spectral data by the azimuthal wave vector direction at each frequency (ϕ_k).
3. Calculate the three components of the electric field from magnetic field observations. This can be done three ways for each component; $E_x(B_x, B_y, B_z)$, $E_y(B_x, B_y, B_z)$, and $E_z(B_x, B_y, B_z)$, as described below.
4. Rotate computed complex amplitudes of electric field back to original field-aligned coordinate system.
5. Transform from original field-aligned coordinates back to antenna aligned coordinates.
6. Compare the amplitude and phase of the observed electric field along each antenna direction with those calculated from magnetic field observations.

To express each component of the wave electric field as a function of each component of the wave magnetic field, we start in a field-aligned coordinate system where the background magnetic field is oriented along the z-direction, and the wave vector k is confined to the x-z plane. The cold plasma wave equation is therefore given by Equation 3 (e.g., Gurnett and Bhattacharjee (2017)).

$$\begin{pmatrix} S - n^2 \cos^2 \theta_k & -iD & n^2 \cos \theta_k \sin \theta_k \\ iD & S - n^2 & 0 \\ n^2 \cos \theta_k \sin \theta_k & 0 & P - n^2 \sin^2 \theta_k \end{pmatrix} \begin{pmatrix} E_x \\ E_y \\ E_z \end{pmatrix} = 0 \quad (3)$$

where S , D , and P are the Stix parameters (Stix, 1992), n is the refractive index, θ_k is the polar angle of the wave vector, and i is the imaginary unit.

This allows us to formulate relations between all components of the electric field, such that;

$$E_x = -\frac{(S - n^2)}{iD} E_y = -\frac{P - n^2 \sin^2 \theta_k}{n^2 \cos \theta_k \sin \theta_k} E_z \quad (4)$$

Faraday's Law ($k \times E = \omega B$) allows us to define the magnetic field in terms of the electric field, such that;

$$B_x = -\frac{k}{\omega} \cos \theta_k E_y \quad (5)$$

$$B_y = \frac{k}{\omega} (\cos \theta_k E_x - \sin \theta_k E_z) \quad (6)$$

$$B_z = \frac{k}{\omega} \sin \theta_k E_y \quad (7)$$

Coupling the cold plasma wave equation with Faraday's Law and $n^2 = \frac{k^2 c^2}{\omega^2}$ allows us to express each component of E as a function of all components of B .

$$E_x = -i \frac{c}{n} \frac{\alpha}{\cos \theta_k} B_x = \frac{c}{n} \frac{\beta}{\beta \cos \theta_k + \gamma \sin \theta_k} B_y = i \frac{c}{n} \frac{\alpha}{\sin \theta_k} B_z \quad (8)$$

$$E_y = -\frac{c}{n \cos \theta_k} B_x = -i \frac{c}{n} \frac{\beta}{\alpha \beta \cos \theta_k + \gamma \alpha \sin \theta_k} B_y = \frac{c}{n \sin \theta_k} B_z \quad (9)$$

$$E_z = i \frac{c}{n} \frac{\alpha \gamma}{\beta \cos \theta_k} B_x = -\frac{c}{n} \frac{\gamma}{\beta \cos \theta_k + \gamma \sin \theta_k} B_y = -i \frac{c}{n} \frac{\alpha \gamma}{\beta \sin \theta_k} B_z \quad (10)$$

where $\alpha = \frac{s-n^2}{D}$, $\beta = P - n^2 \sin^2 \theta_k$, and $\gamma = n^2 \cos \theta_k \sin \theta_k$.

As such, we obtain three independent values for each component of the electric field (e.g., $E_x(B_x)$, $E_x(B_y)$, and $E_x(B_z)$) in field-aligned coordinates. The electric field values are then transformed back into the instrument frame, where the calculated electric field can be directly compared to the observed electric field along each antenna direction. Since all components are complex amplitudes in the frequency domain, this allows for the comparison of both wave amplitude and phase. To ensure sufficient signal in each antenna direction, only observations where both the observed and calculated electric field wave power along each antenna direction exceed $10^{-5} \text{ mV}^2/\text{m}^2\text{Hz}$ are considered in the subsequent analysis.

Note that the SVD technique requires averaging of spectral matrices in order to reliably estimate the planarity of the wave, which is critical information for computing the wave vector direction, which itself is crucial for both accurately transforming between coordinate systems (azimuthal wave vector angle, ϕ_k), and for computing the electric field components from magnetic field observations (polar wave vector angle, θ_k). In order to retain high frequency resolution, we do not want to average the complex Fourier coefficients used in Equations 8–10. Instead SVD analysis is conducted on both the frequency-averaged (averaging over 5 frequency bins) and non-frequency-averaged spectral matrices. This allows us to use the frequency-averaged data to accurately estimate, and filter, by planarity to ensure reliable wave normal estimates, but retain the non-averaged complex Fourier coefficients, as well as increased frequency resolution. The planarity of the frequency-averaged data is assumed to be representative of the non-averaged data within each given frequency range. Furthermore, if the deviation of the wave normal direction computed from the non-averaged and frequency-averaged data exceeds 15° , that observation is removed from our analysis. To estimate the uncertainty in θ_k we considered an example averaged spectral matrix where the SVD determined θ_k was 25.6° and calculated standard deviations of the magnetic spectral matrix components averaged from 5 realizations according to (Priestley, 1989), obtaining a value of 9.38° . Since Priestley (1989) assumes noise matrices, the standard deviation is an upper estimate of the error. As such, an upper estimate of the error in θ_k is $\sim 10^\circ$.

6. Comparing Each Axis of the Measured Electric Field Wave Amplitude and Phase With Theoretical Predictions

Figure 3 shows a direct comparison between the amplitude of the observed and calculated electric field along each antenna direction of the MMS instrumentation for the same three density ranges used in Figure 2. Each row shows the ratio for a different antenna direction: (top) Spin Plane 1, (middle) Spin Plane 2, and (bottom) Spin Axis. Each color distribution represents the electric field calculated from a different component of the magnetic field, with values determined from B_x shown in black, B_y shown in blue, and B_z shown in red. The comparison is presented in the form of a histogram of the ratio between the observed and calculated electric field wave amplitude. The median value of each distribution is provided and all histograms are normalized to peak at unity. Note that in many instances, the black and blue histograms (values calculated from B_x and B_y , respectively) overlap and are indistinguishable.

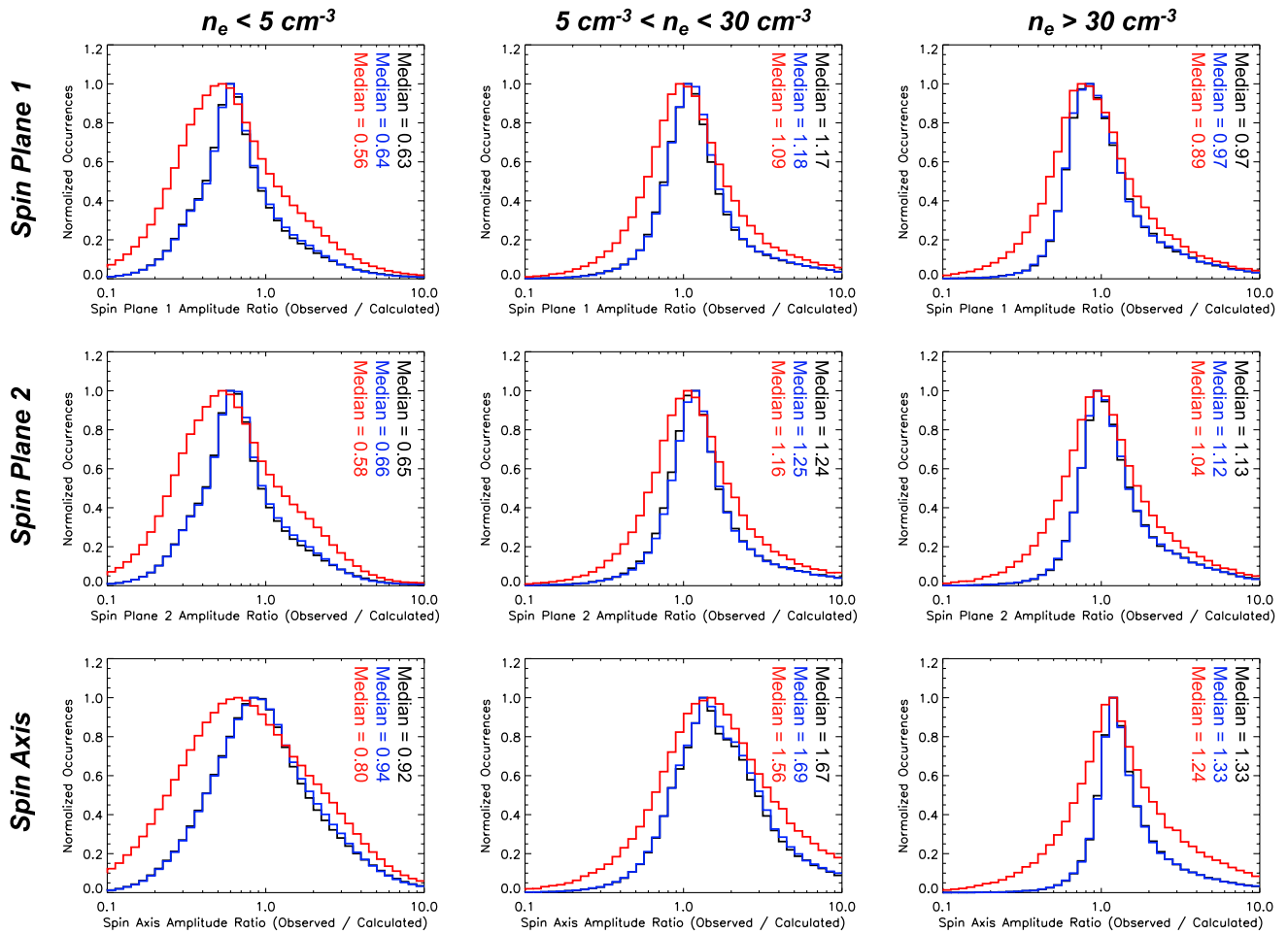


Figure 3. Histograms of the ratio between the observed and calculated electric field wave amplitude for (columns) three different density ranges and (rows) each antenna direction; (top) Spin Plane 1; (middle) Spin Plane 2; and (bottom) Spin Axis. Color represents the component of the magnetic field used in the calculation, (black) B_x , (blue) B_y , and (red) B_z .

For low values of the plasma density ($n_e < 5 \text{ cm}^{-3}$, Figure 3, left column), it can be seen that for the spin plane antennas (top and middle), the distribution of amplitude ratios peaks near 0.6. This is true for both spin plane 1 and spin plane 2, regardless of whether the computed value is determined from B_x , B_y , or B_z . We do note, however, that the distribution determined using B_z (red) is typically broader due to fewer observations where B_z is sufficiently large, since the wave normal direction of whistler-mode waves is often close to field aligned, resulting in only a small electromagnetic component parallel to the background magnetic field in the z-direction. Using these smaller parallel components results in a larger degree of uncertainty in our ratio calculations, which is demonstrated by the larger spread in all distributions presented when using B_z . Overall, these results suggest that, on average, the electric field observed in the spin plane is around 60% of the expected whistler-mode wave amplitude. In contrast, the distribution for the spin axis antenna (bottom) peaks near unity under these conditions, with median values of 0.92 and 0.94 for quantities determined from the perpendicular directions of the magnetic field. These results present both similarities and differences to the analysis performed using Van Allen Probes observations. The amplitude ratio of 0.6 for the spin plane direction is largely similar to that obtained from the Van Allen Probes. However, previous results from the Van Allen Probes identified that the spin axis antenna exhibited larger discrepancies than in the spin plane, with amplitude ratios of 0.1 reported at low densities. MMS results indicate that the observed electric field along the spin axis is largely consistent with what is expected from cold plasma theory. We postulate that these differences are attributable to the different instrumentation and calibration procedures between the two missions.

In intermediate density conditions ($5 \text{ cm}^{-3} < n_e < 30 \text{ cm}^{-3}$, Figure 3, center column), the ratio between the observed and calculated electric field wave amplitude along the spin plane (top and middle) is generally peaked close to, or slightly above, unity. Median ratio values are between 1.09 and 1.25. There also exists a slight difference between the two spin plane antenna directions of the order of $\sim 10\%$. Again, more variation is observed in electric field values determined from B_z (red). These results indicate that the whistler-mode wave amplitude measured along the spin plane is typically 10%–25% greater than what is predicted from magnetic field measurements and cold plasma theory. For the spin axis (bottom), the measured electric field exceeds the expected value by about 55%–70% under these conditions. We note that a similar feature was observed on the Van Allen Probes, with cases where the spin axis over measured the electric field for an intermediate range of densities. This feature is not well understood, and appears not to be spacecraft specific, with both Van Allen Probes and MMS similarly impacted. One possible explanation for the source of this feature was identified for the Polar spacecraft, where instability of the sphere-preamplifier-stub-guard system occurred under a certain set of plasma conditions (Kolesnikova & Béghin, 2001). Note that these median ratio values do vary slightly with the implemented planarity threshold used for wave identification. Several different planarity thresholds were tested, and the general trend was increased planarity thresholds resulted in a slight reduction in the median ratios ($\sim 10\%$), but at the expense of reduced statistics.

When the plasma density is elevated ($n_e > 30 \text{ cm}^{-3}$, Figure 3, right column), the amplitude ratio for the spin plane antennas (top and middle) is peaked very close to unity. Median values range from 0.89 to 1.13. This indicates that the electric field wave amplitude along the spin plane directions is typically in line with the expected value. Similar to the intermediate density regime, we observe subtle differences between the two different spin plane directions on the order of $\sim 10\%$. This is not deemed significant and is attributed to uncertainties in the various coordinate transforms and the assumption of a perfectly planar wave. Along the axis of spin, the measured electric field is, on average, larger than unity, with the distribution of ratios peaking around 1.3. This indicates that the spin axis electric field wave amplitude measured by the spacecraft is $\sim 30\%$ larger than expected. It is worth noting that in all cases, regardless of whether the magnetic field x, y, or z-component has been used in determining the calculated electric field, the ratio distributions are somewhat similar. This demonstrates the robustness of the implemented methodology.

Figure 4 presents a similar analysis but for the phase difference of the whistler-mode wave electric field (observed - calculated). Again, the same three density regimes are represented by the figure columns, and the three different antenna directions are represented by figure rows. Each color represents the component of the magnetic field used in the calculation; B_x (black), B_y (blue), and B_z (red).

In the low-density plasma regime ($n_e < 5 \text{ cm}^{-3}$, Figure 4, left column) the spin plane antennas present only very small phase differences between the observed and calculated electric field, with median values between -5° and -15° . Interestingly, there are slight differences between the two spin plane antenna directions (top and middle panels) of the order of $\sim 5^\circ$ – 10° . Whilst only small, these subtle differences are apparent in the spin plane electric field calculated from all components of the magnetic field (black, blue, and red). For the spin axis (bottom), a more significant phase offset is apparent, with average differences between the observed and expected electric field between -17° and -19° . This result is similar to what has previously been reported for Van Allen Probes observations, with larger phase differences seen in the spin axis measurements compared to the spin plane, particularly at low densities. However, the magnitude of the spin axis phase difference reported here is significantly smaller than the -70° , or larger, phase shifts that were apparent for Van Allen Probes observations.

For intermediate values of the plasma density ($5 \text{ cm}^{-3} < n_e < 30 \text{ cm}^{-3}$, Figure 4, center column) the spin plane electric field (top and middle) distributions are approximately centered on zero, indicating only very small phase differences on average. Median values are between -5° and -8° , indicating very close agreement between observations and theory. For the spin axis (bottom) the phase differences present broad distributions with two peaks; one centered above zero, and one centered below zero. This is due to the presence of a strong dependence of the phase offsets on the frequency of the wave, with lower frequency waves producing positive phase offsets, and higher frequency waves producing negative phase offsets. The transition between positive and negative phase shifts occurs in a relatively narrow frequency range around 100 Hz (Figure S3 provided in Supporting Information S1) which may be attributed to the transition between the resistive and capacitive coupling regimes (R-C transition frequency). Due to the bi-modal nature of the distribution, little useful information is contained in the median values. It is worth noting that in all cases, the black, blue, and red distribution are extremely similar,

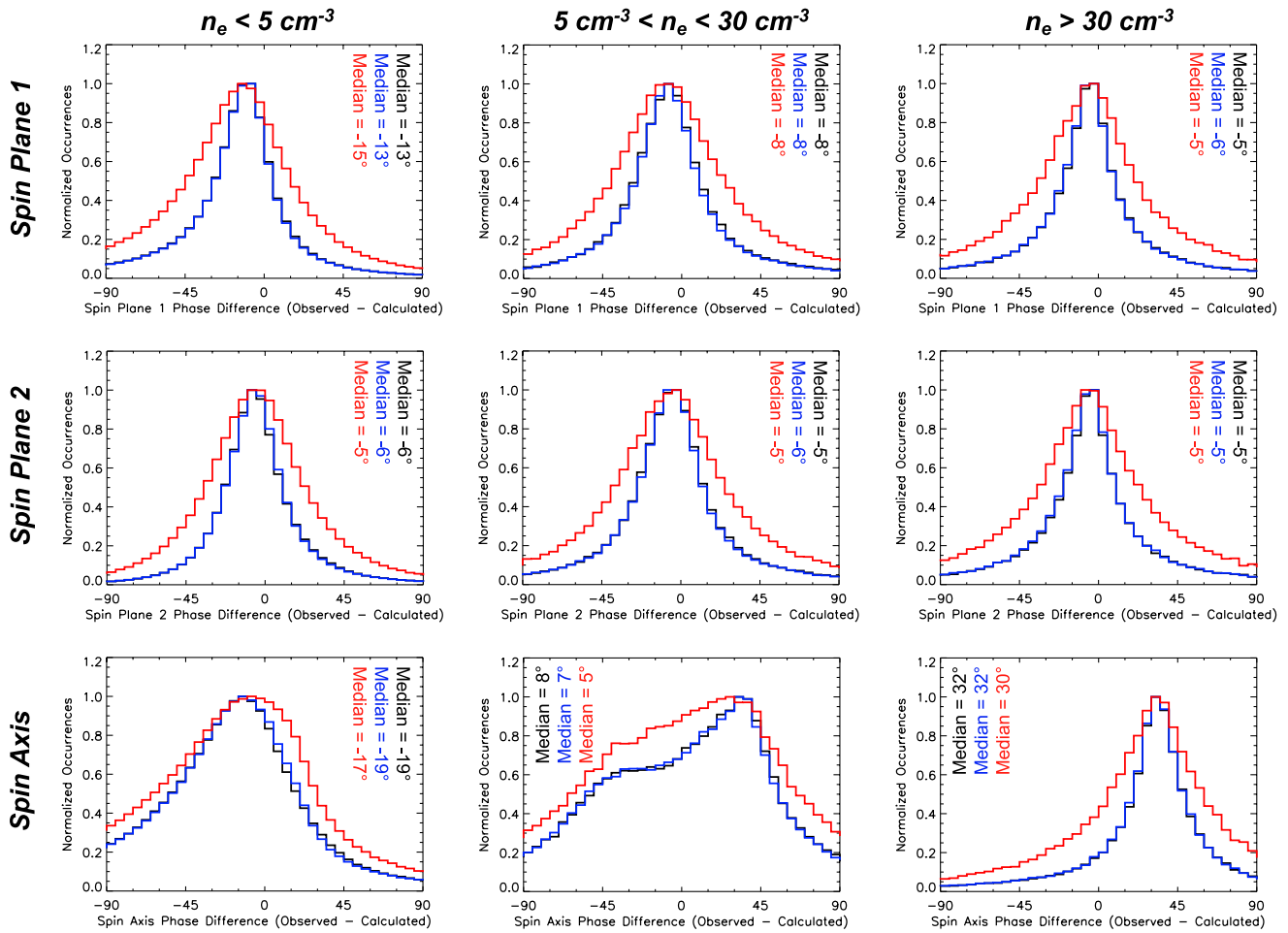


Figure 4. Histograms of the phase difference between the observed and calculated electric field for (columns) three different density ranges and (rows) each antenna direction; (top) Spin Plane 1; (middle) Spin Plane 2; and (bottom) Spin Axis. Color represents the component of the magnetic field used in the calculation, (black) B_x , (blue) B_y , and (red) B_z .

indicating that the electric field can be reliably determined from either the x, y, or z-component of the magnetic field.

In high-density conditions ($n_e > 30 \text{ cm}^{-3}$, Figure 4, right column) the average phase differences determined in the spin plane (top and middle) are both minimal and consistent between all components of the magnetic field used in the calculation. Median values are all close to -5° . This is in contrast to the phase differences in the spin axis observations, where all distributions are peaked close to 30° . We note that positive phase differences are not consistent with antenna-sheath impedance effects, but were also reported in the Van Allen Probes spin axis observations of the electric field. For the Van Allen Probes the maximum reported positive phase shift was 30° , consistent with the values reported here. This effect is not well understood, but has now been demonstrated to be present on multiple high-profile NASA missions. Further investigation of these positive phase shifts is planned as part of future work.

7. Summary and Conclusions

In this study, the variable instrument-plasma coupling interface for the electric field instrumentation onboard MMS has been examined and quantified. First, the angle between the electric and magnetic field associated with whistler-mode waves has been investigated revealing a bifurcated distribution with one peak centered below the expected value of 90° and one peak centered above the expected value of 90° . These two peaks correspond to the propagation direction of the waves past the spacecraft, with one peak attributed to waves propagating with a

component of the Poynting vector parallel to the background magnetic field, and the other peak attributed to anti-parallel propagating waves. This same feature was reported in Van Allen Probes observations, and is direct evidence of sheath impedance effects impacting the measurement of the wave electric field.

To quantify these sheath impedance effects, the whistler-mode wave electric field observed by MMS has been compared to the electric field calculated from magnetic field observations and cold plasma theory. This is initially performed for the total electric field wave amplitude summed over all three measured components, revealing that in low-density conditions, the wave amplitude is approximately 30% less than the expected value, on average. For intermediate and elevated density conditions, the electric field wave amplitude is generally in line with, or marginally greater than, the expected value. These results are very similar to those obtained in previous studies using Van Allen Probes observations, which may be summarized as; (a) the electric field wave amplitude is under-measured in low-density conditions, and (b) the electric field wave amplitude is accurately measured, or slightly over-measured, in the intermediate and high-density regimes.

Furthermore, this study presents a significantly revised technique for determining the wave electric field along each measurement direction of a spacecraft, and applies this technique to MMS observations. Whilst the impact of sheath impedance effects on electric field observations has been previously studied (e.g., Hartley, Christopher et al. (2022); Hartley et al. (2023)), these works were limited in scope due to implemented assumptions. A critical limitation was the required wave, antenna, and magnetic field geometry, with both the antenna orientation and the wave vector required to be approximately parallel to the background magnetic field (within 15°). These criteria were necessary due to the FFTs of the waveform data being performed onboard the Van Allen Probes spacecraft in survey mode, and only the spectral matrices sent to the ground. By using the full waveform observations available in many burst mode data products, limiting the analysis to intervals of favorable geometry is no longer required, thus permitting a more comprehensive investigation. This newly developed technique represents a substantial improvement over previous works due to the removal of multiple limitations, and offers a more general solution for determining the sheath impedance along each antenna direction of, in this case, the MMS electric field instrumentation. This technique may also be applied to other spacecraft missions, including revisiting the Van Allen Probes data, as part of future work.

Applying this revised technique to MMS observations has revealed that the primary source of the under-measurement of the electric field wave amplitude in low-density conditions is the spin-plane antennas, where on average only around 60% of the expected whistler-mode wave amplitude is observed with only a small phase shift. In contrast, spin-axis amplitude measurements in these conditions are, on average, very close to the expected values, within 5%–10%, but with slightly larger phase shifts up to -20° on average. For intermediate density conditions, the spin plane antennas generally observe wave amplitudes that are in agreement, or slightly exceeding, the expected values and with only very small phase differences. In contrast, the spin axis measurement can exceed the expected amplitude by up to 70% and with substantial positive phase shifts for waves above ~ 100 Hz and substantial negative phase shifts for waves below ~ 100 Hz. In the high-density environment, the spin-plane amplitudes are demonstrated to show a high level of agreement with the expected values with very minor phase differences, however measurements along the spin-axis are, on average, over-measured by approximately 30% and with positive phase shifts of $\sim 30^\circ$.

The under-measurement of the electric field under low-density conditions is in agreement with the results obtained from Van Allen Probes, as is the slight over-measurement of wave amplitudes during intermediate and high-density conditions (Hartley, Christopher, et al., 2022). The positive phase shifts at high-density are also consistent with Van Allen Probes results, yet no physical mechanism for producing these phase shifts has been definitively identified. With similar impacts reported on now two NASA missions, we believe that this effect would benefit from dedicated investigative support going forwards. Moreover, there have been multiple recent studies investigating wave-particle interactions at various frequencies by determining energy transfer rates, which directly rely on the measured fluctuations in the electric field (e.g., Afshari et al. (2021, 2024); Chen et al. (2019); Liu (2025)). If electric field observations can be under or over-measured depending on the local plasma environment, this directly impacts these computations of energy exchange rates. As such, taking steps toward a greater understanding of electric field measurements in geospace, as is done in this study, is a crucial step if we are to gain a more complete understanding of the fundamental physical mechanisms that drive particle dynamics.

Conflict of Interest

The authors declare no conflicts of interest relevant to this study.

Availability Statement

All data used during this analysis is freely and publicly available and may be obtained from <https://lasp.colorado.edu/mms/sdc/public/>, or from <https://spdf.gsfc.nasa.gov/pub/data/mms/>. SPASE records for data are (Ergun et al., 2022a, 2022b, 2022c, 2022d) for EDP, (Le Contel et al., 2022a, 2022b, 2022c, 2022d) for SCM, (Russell et al., 2022a, 2022b, 2022c, 2022d) for FGM, and (Gershman et al., 2022a, 2022b, 2022c, 2022d) for FPI. An events list detailing the specific intervals analyzed in this study is available as part of Supporting Information S1.

Acknowledgments

DPH, IWC, MRA and NA acknowledge that this material is based upon work supported by the National Aeronautics and Space Administration under Grant 80NSSC21K0519 issued through the Heliophysics Guest Investigators - Open 2020 Program. OS and IK acknowledge funding from the GACR Grant 25-18095X, and from the Czech MEYS Inter-excellence II programme through project LUAUS23152. IS acknowledges support from the Knut and Alice Wallenberg Foundation.

References

- Afshari, A. S., Howes, G. G., Kletzing, C. A., Hartley, D. P., & Boardsen, S. A. (2021). The importance of electron Landau damping for the dissipation of turbulent energy in terrestrial magnetosheath plasma. *Journal of Geophysical Research: Space Physics*, *126*(12), e2021JA029578. <https://doi.org/10.1029/2021JA029578>
- Afshari, A. S., Howes, G. G., Shuster, J. R., Klein, K. G., McGinnis, D., Martinović, M. M., et al. (2024). Direct observation of ion cyclotron damping of turbulence in Earth's magnetosheath plasma. *Nature Communications*, *15*(1), 7870. <https://doi.org/10.1038/s41467-024-52125-8>
- Bale, S. D., Ullrich, R., Goetz, K., Alster, N., Cecconi, B., Dekkali, M., et al. (2008). The electric antennas for the STEREO/WAVES experiment. *Space Science Reviews*, *136*(1–4), 529–547. <https://doi.org/10.1007/s11214-007-9251-x>
- Bingham, S. T., Moukikis, C. G., Kistler, L. M., Boyd, A. J., Paulson, K., Farrugia, C. J., et al. (2018). The outer radiation belt response to the storm time development of seed electrons and chorus wave activity during CME and CIR driven storms. *Journal of Geophysical Research: Space Physics*, *123*(12), 10139–10157. <https://doi.org/10.1029/2018JA025963>
- Boehm, M. H., Carlson, C. W., McFadden, J. P., Clemmons, J. H., Ergun, R. E., & Mozer, F. S. (1994). Wave rectification in plasma sheaths surrounding electric field antennas. *Journal of Geophysical Research*, *99*(A11), 21361–21374. <https://doi.org/10.1029/94JA01766>
- Bonnell, J. W., Mozer, F. S., Delory, G. T., Hull, A. J., Ergun, R. E., Cully, C. M., et al. (2008). The electric field instrument (EFI) for THEMIS. *Space Science Reviews*, *141*, 303–341. <https://doi.org/10.1007/s11214-008-9469-2>
- Burch, J. L., Moore, T. E., Torbert, R. B., & Giles, B. L. (2016). Magnetospheric multiscale overview and science objectives. *Space Science Reviews*, *199*(1–4), 5–21. <https://doi.org/10.1007/s11214-015-0164-9>
- Califf, S., & Cully, C. M. (2016). Empirical estimates and theoretical predictions of the shorting factor for the THEMIS double-probe electric field instrument. *Journal of Geophysical Research: Space Physics*, *121*(7), 6223–6233. <https://doi.org/10.1002/2016JA022589>
- Chen, C. H. K., Klein, K. G., & Howes, G. G. (2019). Evidence for electron Landau damping in space plasma turbulence. *Nature Communications*, *10*(1), 740. <https://doi.org/10.1038/s41467-019-08435-3>
- Cully, C. M., Ergun, R. E., & Eriksson, A. I. (2007). Electrostatic structure around spacecraft in tenuous plasmas. *Journal of Geophysical Research*, *112*(A9), A09211. <https://doi.org/10.1029/2007JA012269>
- Ergun, R. E., Carlson, C., Mozer, F., Delory, G., Temerin, M., McFadden, J., et al. (2001). The FAST satellite field instrument. *Space Science Reviews*, *98*(1–2), 67–91. <https://doi.org/10.1023/a:1013131708323>
- Ergun, R. E., Lindqvist, P.-A. T., Roy, B., Ahmadi, N., Graham, D., Bruce, B., & James, L. (2022a). MMS 1 Electric Double Probe (EDP) Three-Dimensional Electric Field, Level 2 (L2), Burst Mode, 0.1220703125 ms Data [Dataset]. *Laboratory for Atmospheric and Space Physics; Space Physics Data Facility*. <https://doi.org/10.48322/rxnb-r719>
- Ergun, R. E., Lindqvist, P.-A. T., Roy, B., Ahmadi, N., Graham, D., Bruce, B., & James, L. (2022b). MMS 2 Electric Double Probe (EDP) Three-Dimensional Electric Field, Level 2 (L2), Burst Mode, 0.1220703125 ms Data [Dataset]. *Laboratory for Atmospheric and Space Physics; Space Physics Data Facility*. <https://doi.org/10.48322/pktw-wv31>
- Ergun, R. E., Lindqvist, P.-A. T., Roy, B., Ahmadi, N., Graham, D., Bruce, B., & James, L. (2022c). MMS 3 Electric Double Probe (EDP) Three-Dimensional Electric Field, Level 2 (L2), Burst Mode, 0.1220703125 ms Data [Dataset]. *Laboratory for Atmospheric and Space Physics; Space Physics Data Facility*. <https://doi.org/10.48322/zm13-qd40>
- Ergun, R. E., Lindqvist, P.-A. T., Roy, B., Ahmadi, N., Graham, D., Bruce, B., & James, L. (2022d). MMS 4 Electric Double Probe (EDP) Three-Dimensional Electric Field, Level 2 (L2), Burst Mode, 0.1220703125 ms Data [Dataset]. *Laboratory for Atmospheric and Space Physics; Space Physics Data Facility*. <https://doi.org/10.48322/zpw3-4w58>
- Ergun, R. E., Tucker, S., Westfall, J., Goodrich, K. A., Malaspina, D. M., Summers, D., et al. (2016). The axial Double Probe and fields signal processing for the MMS mission. *Space Science Reviews*, *199*(1), 167–188. <https://doi.org/10.1007/s11214-014-0115-x>
- Fahleson, U. (1967). Theory of electric field measurements conducted in the magnetosphere with electric probes. *Space Science Reviews*, *7*(2–3), 238–262. <https://doi.org/10.1007/bf00215600>
- Gershman, D. J., Giles, B. L., Pollock, C. J., Moore, T. E., & Burch, J. L. (2022a). MMS 1 fast plasma investigation, dual electron spectrometer (FPI, DES) distribution moments, level 2 (L2), Burst mode, 30 ms data [Dataset]. *Laboratory for Atmospheric and Space Physics; Space Physics Data Facility*. <https://doi.org/10.48322/6172-zw20>
- Gershman, D. J., Giles, B. L., Pollock, C. J., Moore, T. E., & Burch, J. L. (2022b). MMS 2 fast plasma investigation, dual electron spectrometer (FPI, DES) distribution moments, level 2 (L2), Burst mode, 30 ms data [Dataset]. *Laboratory for Atmospheric and Space Physics; Space Physics Data Facility*. <https://doi.org/10.48322/tryj-n584>
- Gershman, D. J., Giles, B. L., Pollock, C. J., Moore, T. E., & Burch, J. L. (2022c). MMS 3 fast plasma investigation, dual electron spectrometer (FPI, DES) distribution moments, level 2 (L2), Burst mode, 30 ms data [Dataset]. *Laboratory for Atmospheric and Space Physics; Space Physics Data Facility*. <https://doi.org/10.48322/8ypa-ba28>
- Gershman, D. J., Giles, B. L., Pollock, C. J., Moore, T. E., & Burch, J. L. (2022d). MMS 4 fast plasma investigation, dual electron spectrometer (FPI, DES) distribution moments, level 2 (L2), Burst mode, 30 ms data [Dataset]. *Laboratory for Atmospheric and Space Physics; Space Physics Data Facility*. <https://doi.org/10.48322/20ws-ge68>
- Gurnett, D. A. (1998). Principles of space plasma wave instrument design. In R. F. Pfaff, J. E. Borovsky, & D. T. Young (Eds.), *Measurement techniques in space plasmas fields* (p. 121). AGU. <https://doi.org/10.1002/9781118664391.ch14>

- Gurnett, D. A., & Bhattacharjee, A. (2017). *Introduction to plasma physics: With space, laboratory and astrophysical applications* (2nd ed.). Cambridge University Press. <https://doi.org/10.1017/9781139226059>
- Gustafsson, G., Boström, R., Holback, B., Holmgren, G., Lundgren, A., Stasiewicz, K., et al. (1997). The electric field and wave experiment for the CLUSTER mission. *Space Science Reviews*, 79(1–2), 137–156. <https://doi.org/10.1023/a:1004975108657>
- Hartley, D. P., Chen, L., Christopher, I. W., Kletzing, C. A., Santolík, O., Li, W., & Shi, R. (2022). The angular distribution of lower band chorus waves near plasmaspheric plumes. *Geophysical Research Letters*, 49(9), e2022GL098710. <https://doi.org/10.1029/2022GL098710>
- Hartley, D. P., Chen, L., Gu, W., Christopher, I. W., & Santolík, O. (2025). The impact of plasma density gradients on lower band chorus wave propagation. *Geophysical Research Letters*, 52(6), e2024GL113258. <https://doi.org/10.1029/2024GL113258>
- Hartley, D. P., Chen, Y., Kletzing, C. A., Denton, M. H., & Kurth, W. S. (2015). Applying the cold plasma dispersion relation to whistler mode chorus waves: EMFISIS wave measurements from the Van Allen Probes. *Journal of Geophysical Research: Space Physics*, 120(2), 1144–1152. <https://doi.org/10.1002/2014JA020808>
- Hartley, D. P., Christopher, I. W., Kletzing, C. A., Kurth, W. S., Santolík, O., Kolmašová, I., et al. (2022). Quantifying the sheath impedance of the electric double probe instrument on the Van Allen Probes. *Journal of Geophysical Research: Space Physics*, 127(5), e2022JA030369. <https://doi.org/10.1029/2022JA030369>
- Hartley, D. P., Christopher, I. W., Kletzing, C. A., Kurth, W. S., Santolík, O., Kolmašová, I., et al. (2023). Chorus wave properties from Van Allen Probes: Quantifying the impact of the sheath corrected electric field. *Geophysical Research Letters*, 50(7), e2023GL102922. <https://doi.org/10.1029/2023GL102922>
- Hartley, D. P., Kletzing, C. A., Chen, L., Horne, R. B., & Santolík, O. (2019). Van Allen Probes observations of chorus wave vector orientations: Implications for the chorus-to-hiss mechanism. *Geophysical Research Letters*, 46(5), 2337–2346. <https://doi.org/10.1029/2019GL082111>
- Hartley, D. P., Kletzing, C. A., Kurth, W. S., Bounds, S. R., Averkamp, T. F., Hospodarsky, G. B., et al. (2016). Using the cold plasma dispersion relation and whistler mode waves to quantify the antenna sheath impedance of the Van Allen Probes EFW instrument. *Journal of Geophysical Research: Space Physics*, 121(5), 4590–4606. <https://doi.org/10.1002/2016JA022501>
- Hartley, D. P., Kletzing, C. A., Kurth, W. S., Hospodarsky, G. B., Bounds, S. R., Averkamp, T. F., et al. (2017). An improved sheath impedance model for the Van Allen Probes EFW instrument: Effects of the spin axis antenna. *Journal of Geophysical Research: Space Physics*, 122(4), 4420–4429. <https://doi.org/10.1002/2016JA023597>
- Hartley, D. P., Kletzing, C. A., Santolík, O., Chen, L., & Horne, R. B. (2018). Statistical properties of plasmaspheric hiss from Van Allen Probes observations. *Journal of Geophysical Research: Space Physics*, 123(4), 2605–2619. <https://doi.org/10.1002/2017JA024593>
- Harvey, P., Mozer, F. S., Pankow, D., Wygant, J., Maynard, N. C., Singer, H., et al. (1995). In *The electric field instrument on the polar satellite in the global geospace Mission* (Eds.), C. T. Russell. Kluwer Academic.
- Hospodarsky, G. B. (2016). Spaced-based search coil magnetometers. *Journal of Geophysical Research: Space Physics*, 121(12), 12068–12079. <https://doi.org/10.1002/2016JA022565>
- Khotyaintsev, Y. V., Lindqvist, P.-A., Cully, C. M., Eriksson, A. I., & Andre, M. (2014). In flight calibration of double-probe electric field measurements on Cluster. *Geoscientific Instrumentation, Methods and Data Systems*, 3(2), 143–151. <https://doi.org/10.5194/gi-3-143-2014>
- Kletzing, C. A., Bortnik, J., Hospodarsky, G., Kurth, W. S., Santolík, O., Smith, C. W., et al. (2023). The electric and magnetic fields instrument suite and integrated science (EMFISIS): Science, data, and usage best practices. *Space Science Reviews*, 219(4), 28. <https://doi.org/10.1007/s11214-023-00973-z>
- Kolesnikova, E., & Béghin, C. (2001). Instability problem of the electric field antennas on the Polar spacecraft. *Radio Science*, 36(2), 203–221. <https://doi.org/10.1029/1999RS002303>
- Koons, H. C., McPherson, D. A., & Harbridge, W. B. (1970). Dependence of very-low-frequency electric field antenna impedance on magnetospheric plasma density. *Journal of Geophysical Research*, 75(13), 2490–2502. <https://doi.org/10.1029/JA075i013p02490>
- Lalti, A., Khotyaintsev, Y. V., & Graham, D. B. (2023). Short-wavelength electrostatic wave measurement using MMS spacecraft. *Journal of Geophysical Research: Space Physics*, 128(4), e2022JA031150. <https://doi.org/10.1029/2022JA031150>
- Le Contel, O., Leroy, P., Roux, A., Coillot, C., Alison, D., Bouabdellah, A., et al. (2016). The search-coil magnetometer for MMS. *Space Science Reviews*, 199(1), 257–282. <https://doi.org/10.1007/s11214-014-0096-9>
- Le Contel, O., Torbert, R. B., Mirioni, L., Argall, M. R., & Burch, J. L. (2022a). MMS 1 Search Coil Magnetometer (SCM) AC Magnetic Field Level 2 (L2), Burst Mode, 8192 Sample/s Data [Dataset]. *Laboratory for Atmospheric and Space Physics; Space Physics Data Facility*. <https://doi.org/10.48322/gyvg-pf49>
- Le Contel, O., Torbert, R. B., Mirioni, L., Argall, M. R., & Burch, J. L. (2022b). MMS 2 Search Coil Magnetometer (SCM) AC Magnetic Field Level 2 (L2), Burst Mode, 8192 Sample/s Data [Dataset]. *Laboratory for Atmospheric and Space Physics; Space Physics Data Facility*. <https://doi.org/10.48322/axbs-qh32>
- Le Contel, O., Torbert, R. B., Mirioni, L., Argall, M. R., & Burch, J. L. (2022c). MMS 3 Search Coil Magnetometer (SCM) AC Magnetic Field Level 2 (L2), Burst Mode, 8192 Sample/s Data [Dataset]. *Laboratory for Atmospheric and Space Physics; Space Physics Data Facility*. <https://doi.org/10.48322/mg2d-6848>
- Le Contel, O., Torbert, R. B., Mirioni, L., Argall, M. R., & Burch, J. L. (2022d). MMS 4 Search Coil Magnetometer (SCM) AC Magnetic Field Level 2 (L2), Burst Mode, 8192 Sample/s Data [Dataset]. *Laboratory for Atmospheric and Space Physics; Space Physics Data Facility*. <https://doi.org/10.48322/kp2d-gb32>
- Lejosne, S., & Mozer, F. S. (2019). Shorting factor in-flight calibration for the Van Allen Probes DC electric field measurements in the Earth's plasmasphere. *Earth and Space Science*, 6(4), 646–654. <https://doi.org/10.1029/2018EA000550>
- Li, W., Mourenas, D., Artemyev, A. V., Agapitov, O. V., Bortnik, J., Albert, J. M., et al. (2014). Evidence of stronger pitch angle scattering loss caused by oblique whistler-mode waves as compared with quasi-parallel waves. *Geophysical Research Letters*, 41(17), 6063–6070. <https://doi.org/10.1002/2014GL061260>
- Li, W., Santolík, O., Bortnik, J., Thorne, R. M., Kletzing, C. A., Kurth, W. S., & Hospodarsky, G. B. (2016). New chorus wave properties near the equator from Van Allen Probes wave observations. *Geophysical Research Letters*, 43(10), 4725–4735. <https://doi.org/10.1002/2016GL068780>
- Lindqvist, P.-A., Olsson, G., Torbert, R. B., King, B., Granoff, M., Rau, D., et al. (2016). The spin-plane Double Probe electric field instrument for MMS. *Space Science Reviews*, 199(1), 137–165. <https://doi.org/10.1007/s11214-014-0116-9>
- Liu, C. M., Zhao, B. N., Cao, J. B., Pollock, C. J., Russell, C. T., Liu, Y. Y., et al. (2025). Field-particle energy transfer during chorus emissions in space. *Nature*, 637(8047), 813–820. <https://doi.org/10.1038/s41586-024-08402-z>
- Marklund, G. (1993). Viking investigations of auroral electrodynamic processes. *Journal of Geophysical Research*, 98(A2), 1691–1704. <https://doi.org/10.1029/92ja01518>
- Marklund, G., André, M., Lundin, R., & Grahn, S. (2004). The Swedish small satellite program for space plasma investigations. *Space Science Reviews*, 111(3–4), 377–413. <https://doi.org/10.1023/b:spac.0000032690.82775.d8>

- Mauk, B., Fox, N. J., Kanekal, S., Kessel, R., Sibeck, D., & Ukhorskiy, A. (2012). Science objectives and rationale for the Radiation Belt Storm Probes mission. In *The Van Allen probes Mission* (pp. 3–27). Springer.
- Mozer, F. S. (1973). *A proposal to measure quasi-static electric fields on the ISEE-1 mother daughter satellite* (Technical Note, UCBSL No. 454). University of California Berkeley Space Science.
- Mozer, F. S., Berthelier, J.-J., Fahlson, U. V., & Fälthammar, C.-G. (1974). *A proposal to measure the quasi-static vector electric field on the low altitude and the elliptic orbiting electrodynamic explorer satellites*. Research Proposal to the National Aeronautics and Space Administration.
- Mozer, F. S., Cattell, C., Temerin, M., Torbert, R., Von Glinski, S., Woldorff, M., & Wygant, J. (1979). The dc and ac electric field, plasma density, plasma temperature, and field-aligned current experiments on the S3-3 satellite. *Journal of Geophysical Research*, *84*(A10), 5875–5884. <https://doi.org/10.1029/JA084iA10p05875>
- Pedersen, A., Mozer, F., & Gustafsson, G. (1998). Electric field measurements in a tenuous plasma with spherical double probes. In *Measurement techniques in space plasmas: Fields. Geophysical Monograph 103*. AGU.
- Pollock, C., Moore, T., Jacques, A., Burch, J., Gliese, U., Saito, Y., et al. (2016). Fast plasma investigation for magnetospheric multiscale. *Space Science Reviews*, *199*(1–4), 331–406. <https://doi.org/10.1007/s11214-016-0245-4>
- Priestley, M. B. (1989). *Spectral analysis and time series*. Academic Press, 702.
- Russell, C. T., Magnes, W., Wei, H., Bromund, K. R., Plaschke, F., Fischer, D., et al. (2022a). MMS 1 Flux Gate Magnetometer (FGM) DC Magnetic Field, Level 2 (L2), Burst Mode, 128 Sample/s, v4/5 data [Dataset]. *Laboratory for Atmospheric and Space Physics; Space Physics Data Facility*. <https://doi.org/10.48322/pj0n-m695>
- Russell, C. T., Anderson, B. J., Baumjohann, W., Bromund, K. R., Dearborn, D., Fischer, D., et al. (2016). The magnetospheric multiscale magnetometers. *Space Science Reviews*, *199*(1), 189–256. <https://doi.org/10.1007/s11214-014-0057-3>
- Russell, C. T., Magnes, W., Wei, H., Bromund, K. R., Plaschke, F., Fischer, D., et al. (2022b). MMS 2 Flux Gate Magnetometer (FGM) DC Magnetic Field, Level 2 (L2), Burst Mode, 128 Sample/s, v4/5 data [Dataset]. *Laboratory for Atmospheric and Space Physics; Space Physics Data Facility*. <https://doi.org/10.48322/ggx2-zg64>
- Russell, C. T., Magnes, W., Wei, H., Bromund, K. R., Plaschke, F., Fischer, D., et al. (2022c). MMS 3 Flux Gate Magnetometer (FGM) DC Magnetic Field, Level 2 (L2), Burst Mode, 128 Sample/s, v4/5 data [Dataset]. *Laboratory for Atmospheric and Space Physics; Space Physics Data Facility*. <https://doi.org/10.48322/y55w-eb74>
- Russell, C. T., Magnes, W., Wei, H., Bromund, K. R., Plaschke, F., Fischer, D., et al. (2022d). MMS 4 Flux Gate Magnetometer (FGM) DC Magnetic Field, Level 2 (L2), Burst Mode, 128 Sample/s, v4/5 data [Dataset]. *Laboratory for Atmospheric and Space Physics; Space Physics Data Facility*. <https://doi.org/10.48322/257w-3j79>
- Santolík, O., Kolmašová, I., Taubenschuss, U., Hanzelka, M., & Hartley, D. P. (2025). A dataset of lower band Whistler mode chorus and exohiss with instrumental noise thresholds. *Scientific Data*, *12*(1), 1265. <https://doi.org/10.1038/s41597-025-05531-6>
- Santolík, O., Parrot, M., & Lefeuvre, F. (2003). Singular value decomposition methods for wave propagation analysis. *Radio Science*, *38*, 1010. <https://doi.org/10.1029/2000rs002523>
- Santolík, O., Pickett, J. S., Gurnett, D. A., Menietti, J. D., Tsurutani, B. T., & Verkhoglyadova, O. (2010). Survey of Poynting flux of whistler mode chorus in the outer zone. *Journal of Geophysical Research*, *115*(A7), A00F13. <https://doi.org/10.1029/2009JA014925>
- Santolík, O., Pickett, J. S., Gurnett, D. A., & Storey, L. R. O. (2002). Magnetic component of narrowband ion cyclotron waves in the auroral zone. *Journal of Geophysical Research*, *107*(A12), 1444. <https://doi.org/10.1029/2001JA000146>
- Stix, T. H. (1992). Waves in plasmas. *American Inst. of Physics*.
- Storey, L. R. O. (1963). The design of an electric dipole antenna for VLF reception within the ionosphere. *Centre National D'Etudes des Telecommunications, Dep. Tele-commande*.
- Svenningsson, I., Yordanova, E., Cozzani, G., Khotyaintsev, Y. V., & André, M. (2022). Kinetic generation of whistler waves in the turbulent magnetosheath. *Geophysical Research Letters*, *49*(15), e2022GL099065. <https://doi.org/10.1029/2022GL099065>
- Svenningsson, I., Yordanova, E., Khotyaintsev, Y. V., André, M., Cozzani, G., & Steinvall, K. (2024). Whistler waves in the quasi-parallel and quasi-perpendicular magnetosheath. *Journal of Geophysical Research: Space Physics*, *129*(6), e2024JA032661. <https://doi.org/10.1029/2024JA032661>
- Taubenschuss, U., Santolík, O., Breuillard, H., Li, W., & Le Contel, O. (2016). Poynting vector and wave vector directions of equatorial chorus. *Journal of Geophysical Research: Space Physics*, *121*(12), 11912–11928. <https://doi.org/10.1002/2016JA023389>
- Torbert, R. B., Russell, C. T., Magnes, W., Ergun, R. E., Lindqvist, P. A., LeContel, O., et al. (2016). The FIELDs instrument suite on MMS: Scientific objectives, measurements, and data products. *Space Science Reviews*, *199*(1), 105–135. <https://doi.org/10.1007/s11214-014-0109-8>
- Toy-Edens, V., Mo, W., Raptis, S., & Turner, D. L. (2024). Classifying 8 years of MMS dayside plasma regions via unsupervised machine learning. *Journal of Geophysical Research: Space Physics*, *129*(6), e2024JA032431. <https://doi.org/10.1029/2024JA032431>
- Wygant, J. R., Bonnell, J. W., Goetz, K., Ergun, R. E., Mozer, F. S., Bale, S. D., et al. (2013). The electric field, and waves (EFW) instruments on the radiation belt storm probes Mission. *Space Science Reviews*. <https://doi.org/10.1007/s1124-013-0013-7>
- Wygant, J. R., Harvey, P. R., Pankow, D., Mozer, F. S., Maynard, N., Singer, H., et al. (1992). The CRRES electric field experiment/Langmuir probe. *Journal of Spacecraft and Rockets*, *29*(4), 601–604. <https://doi.org/10.2514/3.25507>